Evolution of porosity and diffusivity associated with chemical weathering of a basalt clast

Alexis Navarre-Sitchler,[1,3] Carl I. Steefel,[2,3] Li Yang,[2,3] Liviu Tomutsa,[2] and Susan L. Brantley[3,4]

[1] Weathering of rocks as a result of exposure to water and the atmosphere can cause significant changes in their chemistry and porosity. In low-porosity rocks, such as basalts, changes in porosity, resulting from chemical weathering, are likely to modify the rock's effective diffusivity and permeability, affecting the rate of solute transport and thus potentially the rate of overall weathering to the extent that transport is the rate limiting step. Changes in total porosity as a result of mineral dissolution and precipitation have typically been used to calculate effective diffusion coefficients through Archie's law for reactive transport simulations of chemical weathering, but this approach fails to account for unconnected porosity that does not contribute to transport. In this study, we combine synchrotron X-ray microcomputed tomography (μCT) and laboratory and numerical diffusion experiments to examine changes in both total and effective porosity and effective diffusion coefficients across a weathering interface in a weathered basalt clast from Costa Rica. The μCT data indicate that below a critical value of $\sim$9%, the porosity is largely unconnected in the basalt clast. The μCT data were further used to construct a numerical pore network model to determine upscaled, effective diffusivities as a function of total porosity (ranging from 3 to 30%) for comparison with diffusivities determined in laboratory tracer experiments. By using effective porosity as the scaling parameter and accounting for critical porosity, a model is developed that accurately predicts continuum-scale effective diffusivities across the weathering interface of the basalt clast.

Citation: Navarre-Sitchler, A., C. I. Steefel, L. Yang, L. Tomutsa, and S. L. Brantley (2009), Evolution of porosity and diffusivity associated with chemical weathering of a basalt clast, *J. Geophys. Res.*, *114*, F02016, doi:10.1029/2008JF001060.

1. Introduction

[2] The dissolution and precipitation of minerals during weathering not only changes the chemistry of rocks, but also their physical properties such as porosity, permeability, effective diffusivity, compressive strength, and tensile strength [e.g., *Lumb*, 1983; *Tugrul*, 2004; *Fletcher et al.*, 2006]. The products of bedrock weathering, detrital rock material and dissolved ions, contribute to important environmental processes including landform development, nutrient cycling in soils and rivers, sedimentation that ultimately leads to oil and gas generation, and the regulation of atmospheric CO_2 over geologic time scales. Despite its importance to many environmental processes, rock weathering and the formation of saprolite, rock that is chemically weathered in situ, are not well understood partly because of the difficulty in understanding complex interactions between physical and chemical processes. Our inability to link chemical and mineralogical changes within a weathering environment to the evolution of physical features such as porosity, effective diffusivity, and permeability hinders our understanding of the important process of saprolite/sediment formation from bedrock weathering.

[3] In weathering systems, the pore network is arguably the most important physical characteristic of a rock because it provides pathways for water flow or infiltration and solute transport. The permeability and diffusivity of porous media are functions of the geometry of the pore network that is described in terms of the total porosity, tortuosity, pore throat size, and pore/mineral interfacial area. Chemical weathering reactions can induce changes in the pore network geometry and can therefore change the rates of fluid transport, and thus potentially the overall rates of mineral weathering [e.g., *Lebedeva et al.*, 2007; *Fletcher et al.*, 2006]. Differences between laboratory and field systems in terms of their mineral surface area and transport properties are two of the potential sources of the observed $2-6$ order of magnitude difference between rates determined in these

[1]Department of Geology and Geophysics, University of Wyoming, Laramie, Wyoming, USA.
[2]Earth Sciences Division, Lawrence Berkeley National Laboratory, Berkeley, California, USA.
[3]Center for Environmental Kinetics Analysis, Pennsylvania State University, University Park, Pennsylvania, USA.
[4]Earth and Environmental Systems Institute, Pennsylvania State University, University Park, Pennsylvania, USA.

systems [e.g., *Velbel*, 1993; *White and Brantley*, 1995; *Navarre-Sitchler and Brantley*, 2007; *Maher et al.*, 2006; *White*, 2008; *Brantley*, 2008]. Therefore, a fundamental understanding of how the pore network evolves with mineral dissolution and precipitation is necessary for predicting field processes from laboratory dissolution kinetics [*Navarre-Sitchler and Brantley*, 2007].

[4] The coupling of reaction and transport in numerical models [e.g., *Steefel and Lasaga*, 1994; *Lichtner*, 1996] has made it possible to study the impacts of mineral dissolution and precipitation on fluid transport in important environmental systems such as bedrock weathering. Two complementary modeling techniques used to study changes in transport as a result of mineral alteration are pore network models and continuum models [*Steefel et al.*, 2005]. Pore network models are used to model processes at the pore scale, while continuum models are generally used to model processes at larger scales where average properties such as porosity, permeability, and diffusivity are defined. One of the differences between these modeling techniques is that pore network models explicitly consider pore geometry and spatial distribution when calculating mass transport, while continuum models do not except in some average sense. For example, there is no need to define an effective porosity or diffusivity within a grid cell corresponding to a discrete pore in a pore network model; the porosity is equal to one and the diffusivity is equal to that of the solute of interest in water. While pore network models can be used to explicitly investigate porosity changes at the pore-scale, continuum models are better suited for modeling large-scale problems, such as weathering at the soil profile or watershed scale. Single continuum modeling efforts are now being used to interpret weathering in field systems [*Maher et al.*, 2006; *Hausrath et al.*, 2008; *Moore*, 2008; *Sitchler*, 2008]. The results from these modeling efforts indicate a need to understand changes in mineral surface area and fluid transport (parameters that are influenced by porosity) with weathering. Thus, relationships are required to extrapolate processes occurring at the scale of the pore network up to the continuum scale. Scaling of such processes can be achieved through multicontinuum models or functional relationships such as Archie's law.

[5] In continuum models, effective upscaled transport parameters such as effective diffusivity and hydraulic conductivity are used to extrapolate pore-scale processes up to the continuum scale [*Saripalli et al.*, 2001; *Steefel et al.*, 2005]. When determining effective transport parameters in porous rocks at the continuum scale, it is necessary to account for tortuosity (τ), defined as the ratio of the path length the solute would flow in water alone, L, relative to the tortuous path it follows through the rock, L_e [*Bear*, 1972]

$$\tau (L/L_e)^2. \tag{1}$$

According to this definition, tortuosity is always <1 (the inverse of equation (1) has also been used). If the tortuosity is known, the effective diffusion coefficient (D_e, cm^2 s^{-1}) in porous media can be calculated from equation (2)

$$D_e = \tau D_0, \tag{2}$$

where D_o is the diffusion coefficient in pure water (cm^2 s^{-1}). Tortuosity, however, changes with changing porosity [*Shen and Chen*, 2007] and pore geometry as weathering progresses. Therefore, in models of diffusion-dominated weathering systems where porosity is allowed to vary with reaction, a functional relationship between porosity and the effective diffusivity is defined. A common way to do so is by using Archie's law [*Archie*, 1942; *Oelkers*, 1996]. Archie's law is used to estimate the effective diffusion coefficient of porous media (D_e, cm^2 s^{-1}) according to

$$D_e = D_o \phi^m, \tag{3}$$

where ϕ is the measured total porosity of the porous media and m is the cementation exponent determined experimentally by fitting data describing diffusivity and porosity for multiple samples [*Dullien*, 1992]. Values of the cementation exponent vary in geological samples from 1.33 for diffusive gas in soils to 5.4 for diffusive transport of water in clays [*Millington and Quirk*, 1964; *Ullman and Aller*, 1982; *Adler et al.*, 1992; *Oelkers*, 1996]. The porosity in equation (3) may either be measured as total or effective porosity depending on the sample characteristics and measurement methods. Effective porosity is all porosity that is connected and available for fluid transport [*Tarafdar and Roy*, 1998]

$$\phi_e = \varepsilon \phi_T. \tag{4}$$

Here, ε is the connectivity, or fraction of total porosity contained in pathways that are connected across a sample (values range from 0 to 1) and ϕ_T is the total porosity of the sample. The distinction between total and effective porosity is important because only changes in total porosity are typically tracked as a result of mineral alteration in continuum reactive transport models. Therefore, total porosity in these models is used to estimate effective diffusion coefficients.

[6] The water saturation method is commonly used to measure porosity in geological samples. However, in systems containing dead-end and isolated pores, not all of the porosity is connected and accounted for when using this method. It has been shown that models better predict diffusion experiments in granite when dead-end pores are accounted for [*Lever et al.*, 1985]. Interpretations of diffusion experiments with Archie's law are not consistent in the use of either total or effective porosity [*Tarafdar and Roy*, 1998]. For example, in the study of *Boving and Grathwohl* [2001] porosity is measured by water saturation methods. Therefore, the porosity measured is likely effective porosity not total porosity, but a distinction is not made between total and effective porosity in the analysis of the diffusion experiments. In this study, *Boving and Grathwohl* [2001] report a cementation exponent of 2.2 for sandstones and carbonates ranging in porosity from 3.7 to >40%. It is unclear whether effective diffusion coefficients scale with total or effective porosity in this study. These authors do suggest that Archie's law describes the relationship between porosity and effective diffusion coefficients better in the high-porosity samples where effects of dead-end and isolated pores are minor compared to the low-porosity samples. Here we examine the difference between using total porosity and effective porosity as the scaling parameter in Archie's law when estimating D_e across a weathering interface in basalt.
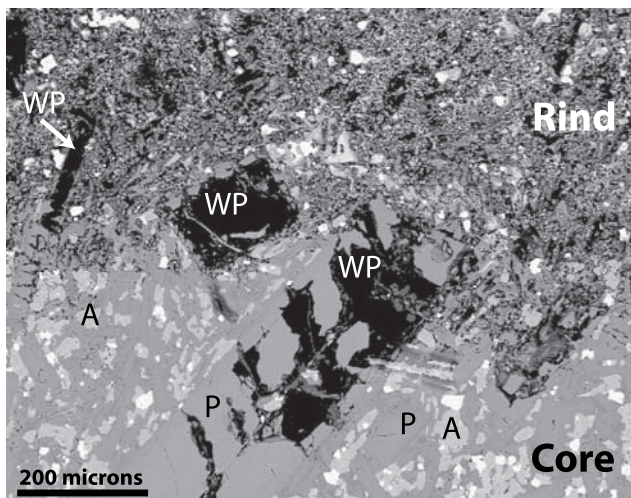
Figure 1. Scanning electron microscope backscatter image of one of the basalt clasts that electron microprobe data was collected for imaged across the reaction front. Labels are as follows: P, plagioclase; WP, weathered plagioclase; A, augite. Pores are black. There is a sharp contrast in porosity between the core and the rind as a result of dissolution of primary minerals. A large plagioclase crystal in the middle of the image is beginning to dissolve and create secondary porosity. Where other plagioclase crystals have dissolved, pores also remain.

[7] The weathering of basalt is of particular interest because it is one of the fastest weathering silicate rocks. Furthermore, approximately 8.5% of the surface area of silicate rock at Earth's surface is basaltic [*Amiotte-Suchet et al.*, 2003]. Almost thirty five percent of continental CO_2 consumption by silicate weathering is due to basalt [*Dessert et al.*, 2003; *Navarre-Sitchler and Brantley*, 2007]. Since transport through low-porosity crystalline rocks is typically very slow in the absence of fractures [*Lebedeva et al.*, 2007], the evolution of the pore network and diffusivity during chemical weathering is integral to the weathering process. An understanding of how the pore network and diffusivity evolve can help predict rates of basalt weathering in natural systems. Here, we use pore connectivity as an indicator of changes to the pore network and quantify the relationship between total and effective porosity using synchrotron X-ray microcomputed tomography (μCT) images of the weathered basalt clasts. Computed tomography has proven to be a useful, nondestructive technique for imaging porosity in complex lithologies [*Ketcham and Iturrino*, 2005]. We then relate the porosity to estimated effective diffusion coefficients at different stages of weathering as determined from experimental and numerical tracer diffusion experiments. These techniques allow us to quantify in situ changes in both total and effective porosity resulting strictly from the chemical dissolution of parent minerals during bedrock weathering.

2. Sample Description

[8] Weathering rinds, permeable crusts enriched in immobile oxides (i.e., Fe_2O_3, TiO_2, and Al_2O_3) that envelop unweathered cores of rock [*Colman and Pierce*, 1981; *Sak et al.*, 2004], provide a unique natural environment where chemical weathering processes occur in the absence of physical erosion. Using weathering rinds we can study weathering processes at the core/rind interface in detail at high spatial resolution and over long time periods where clasts subjected to differing periods of weathering are available [*Colman and Pierce*, 1981; *Oguchi and Matsukura*, 2000; *Sak et al.*, 2004]. Studying weathering in this small-scale weathering system removes many of the complicating factors of larger-scale field studies such as fracturing, heterogeneity in parent material, and differences in microclimate. As a result we are able to focus our experiments and analysis on a single aspect of bedrock weathering, porosity development due solely to mineral dissolution.

[9] Weathered basalt clasts were collected in Costa Rica from an alluvial terrace deposited approximately 125 ka [*Sak et al.*, 2004]. The basaltic parent material is primarily plagioclase (67%) and augite (27%) with trace amounts of silicate glass (2%), ilmenite (2%) and magnetite (1%). Plagiocase and augite occur both as fine-grained matrix and as larger phenocrysts (up to $\sim$ 50 μm diameter for the augites and several hundred μm in length for the long axis of the plagioclase, see Figure 1). The basalt clasts weather when precipitation advects through the matrix material in the terrace and comes into contact with the parent basalt clasts. The basalts are very low porosity (1–3%) and advective flow through the basalt is thus likely to be insignificant. Instead, mass transfer of reactants and products to or from the weathering interface probably occurs by diffusion.

[10] The weathering products found in the rind are goethite (FeOOH), gibbsite ($Al(OH)_3$), and trace amounts of kaolinite ($Si_2Al_2O_5(OH)_4$). On the basis of a variety of observations [see *Sak et al.*, 2004; *Hausrath et al.*, 2008] iron oxide precipitation around augite crystals is the first evidence of alteration in the clast. Plagioclase is the first mineral to dissolve and create secondary porosity but is accompanied by augite dissolution soon after the feldspar dissolution is initiated. Evidence of this is shown in backscatter electron images collected using a scanning electron microscope of the interface between the unweathered core and rind (Figure 1). The core/rind interface advances into the unweathered basalt at a rate of $\sim$0.4 mm ka^{-1} [*Pelt et al.*, 2009]. The dissolution of parent minerals and mass removal from the system through aqueous transport results in a density decrease from 2.8 g cm^{-3} in the core to $\sim$1 g cm^{-3} in the rind [*Sak et al.*, 2004]. This decrease in density corresponds to an increase in porosity from about 3 to 50% [*Sak et al.*, 2004].

3. Methods
3.1. Chemical Profiles Across Core-Rind Transition

[11] Bulk chemical compositions were analyzed by electron microprobe (EMP) across the reaction front of two basalt clasts. Profiles measured on polished thin sections, cut to be 4 mm in length and oriented perpendicular to the weathering interface, were analyzed by measuring compositions at 50 micron sized spots positioned along linear transects across the weathering interface with 50 micron spacing. Eight to ten profiles on each clast were collected
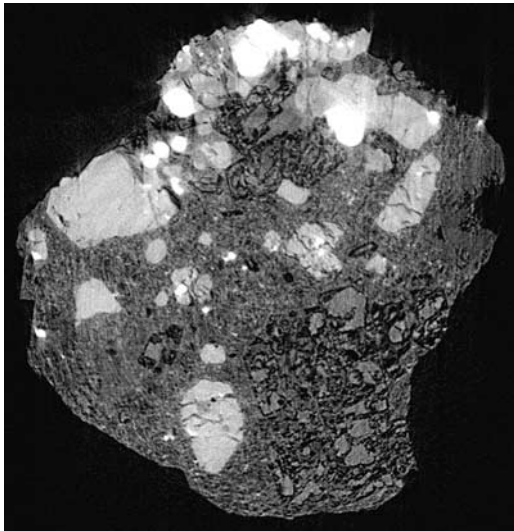
Figure 2. Two-dimensional image reconstructed from μCT data collected near the weathering interface of a weathering rind developed on a basalt clast from the 125 ka terrace. Dark areas are relatively less dense than light areas (black areas show porosity). All images rendered from the μCT data are provided in the auxiliary material.[1]

parallel to each other at 100 micron spacing and averaged to determine bulk chemical changes across the weathering front.

3.2. Quantification of Total Porosity and Pore Connectivity

[12] An intact cylindrical sample, 4 mm in diameter and oriented approximately perpendicular to the weathering interface was drilled out of a basalt clast from the 125 ka terrace. This sample was oriented approximately perpendicular to the core-rind interface and contained material from the unweathered basalt through the interface into the weathering rind. The rind material closer to the outer surface of the weathered clast is extremely weathered and highly porous, making it too unconsolidated to sample through core drilling. Density in this sample was imaged as a function of position using synchrotron X-ray-based 3-D microcomputed tomography (Beamline 8.3.2 at the Advanced Light Source at Lawrence Berkeley National Laboratory) with 4.4 micron resolution. Computed tomography is used to image density differences by illuminating a rotating sample with a beam of 25kev energy X-rays. As these X-rays pass through the sample, they are attenuated as a function of the density of the material, with lower-density material attenuating the X-rays less. By rotating the sample while measuring the intensity of the transmitted X-rays, a large number of radiographs (projections) are acquired. From these projections 2-D images (slices) of the relative density of the sample are reconstructed (Figure 2). A 3-D image of the relative density of a sample is obtained by stacking slices on top of each other. Since porosity (air) attenuates the X-ray transmission less than the minerals in the sample, these

data provide a nondestructive method for quantifying and mapping distribution of porosity in the sample within the limits of the resolution of the instrument (4.4 microns).

[13] With further analysis, each voxel (3-D pixel) in the image is assigned a computed tomography (CT) number that indicates the relative attenuation of X-rays from 0 for no attenuation (air) to >3 for Fe-Ti oxides, the densest material in the basalt. These CT numbers, after rescaling to values from 0 (air) to 1 (Fe-Ti oxide), were then multiplied by 255 to convert to common $0-255$ gray scale. CT numbers less than 45 using the rescaled gray-scale values were defined as porosity, while those above 45 were defined as minerals. This attribution is consistent with both qualitative visual inspection of the images and histograms of the data (Figure 3).

[14] The CT data were sampled in two sizes of cubes, 110 and 220 μm on a side, to analyze the porosity in the unweathered basalt and across the core-rind interface. An area in the unweathered basalt was chosen randomly and then samples were taken sequentially from that point in the unweathered basalt in a line perpendicular to the core-rind interface from the unweathered to the weathered basalt across the interface. Additionally, a larger sample of CT data from the unweathered basalt, 1.1 mm on a side, was also analyzed. Total porosity (ϕ_T, expressed as a percent) was defined as the fraction of voxels within a sample with a CT number less than 45. A burning algorithm in the code Percolate [*Bentz and Garboczi*, 1992] was used to calculate the connectivity, ε ($0 < \varepsilon < 1$), or fraction of total porosity contained in pathways connected from one side of the sample to the other. A burning algorithm starts on one side of a sample in a pore voxel and "burns" that pixel by setting the gray-scale number of that voxel to one outside of the range of the data set. Any pore that touches the first pore is also "burned" in the same fashion and this continues across the sample grid [*Garboczi et al.*, 1999]. For each sample connectivity was measured along all three axes and these connectivity values averaged for the total sample connectivity. The effective porosity (ϕ_e) of each sample is calculated from the connectivity using equation (4).

3.3. Laboratory Tracer Diffusion Experiments

[15] Diffusion experiments using bromide as a tracer were performed on 3 samples of unweathered basalt (DP3, DP6, and DP5u) and 1 sample of weathered basalt (DP5w). Rectangular samples ($1 \times 5 \times 50$ mm) were cut from 3 different basalt clasts from terrace Qt2 and glued on ceramic sample cast holders with crystal[R] thermal glue, leaving only one end of the sample open to bromide tracer solutions by protecting other surfaces of the sample during the diffusion experiment (Figure 4). The mounted sample units (samples plus the ceramic sample holders, except the front ceramic cover) were oven dried at 50°C, and then placed into a stainless steel vacuum chamber at high vacuum for several hours. Samples were then injected with 0.5M potassium chloride (KCl) solution and were kept under 5 atm N_2 to ensure saturation of the sample with KCl solution. Once saturated with KCl, the top surface of the sample was sealed with a uniform layer of weathering resistant tape (3M[R] 836, about 50 microns in thickness) to allow the transmission of X-ray fluorescence signal. Another protective rubber gasket sheet was further placed

---

CT value (0.176) separating pores and matrix minerals
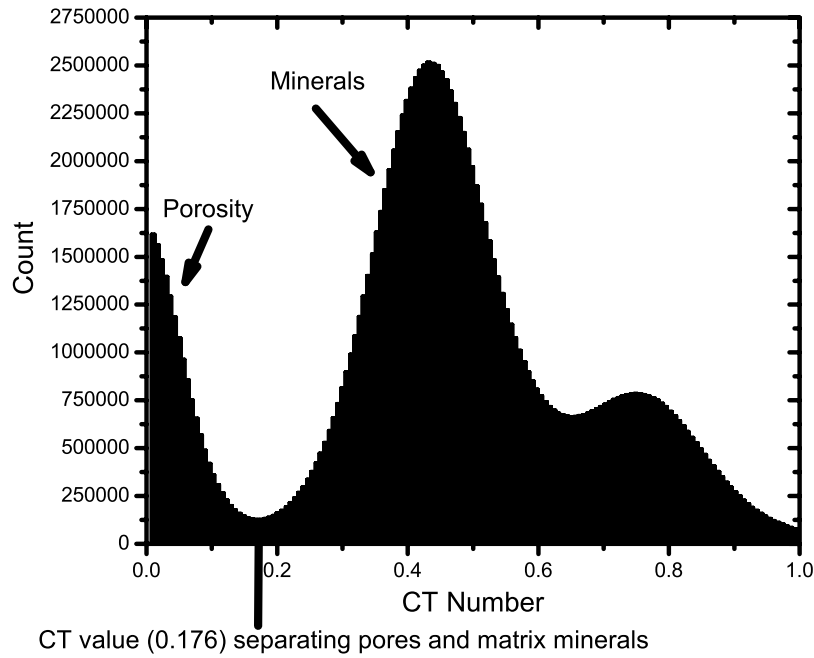
Figure 3. Histogram of number of values measured (count) for each CT number in a volume of 1.33 mm^3 in the unweathered basalt. On the basis of the bimodal distribution of this data, CT numbers less then 0.175 (45 when rescaled to values from 1 to 255 as described in text) are considered to be porosity and numbers greater than this value are considered to be mineral grains.

between the sealed top surface and the front ceramic cover. The assembled sample units were then tightly clamped together with 3 clamps and placed into 500 ml of degassed 0.5 M KBr solution. With this arrangement, only one face, measuring 1 by 5 mm, at the end of the sample was exposed to the tracer solution.

[16] The concentration profiles of bromide were measured at 7 days for sample DP5 and at 17 and 34 days for samples DP3 and DP6 by measuring the bromide fluorescence signals across the top surface of the sample, after removing the ceramic cover and rubber protective sheet, using synchrotron micro-X-ray fluorescence (μXRF) mapping. The synchrotron μXRF scans were performed on Beamline 10.3.2 at the Advanced Light Source (ALS) of Lawrence Berkeley National Laboratory. Samples were scanned with an incoming energy of 13.7 KeV, 50 ms count time and a step size of 20 microns. The Br fluorescence signal was collected with a 7 element Germanium solid state detector.

[17] For each concentration profile, the effective diffusion coefficient (D_e, cm^2 s^{-1}) was calculated by fitting a diffusion equation to the measured concentration where the concentration of Br in the porous media (C) reached half that of the original diffusing fluid (C_o, i.e., $(C/C_o) = 0.5$) outside of the sample at time (t, s)

$$C/C_o = erfc\left(x/2\sqrt{D_e t}\right). \qquad (5)$$

Here, x is the distance in cm into the sample where a Br concentration of half the original concentration was measured.

3.4. Pore Network Modeling of Tracer Diffusion

[18] CrunchFlow (www.csteefel.com) was used to model the diffusion experiments using both 1-D and 3-D simulations. The 1-D models assume a homogeneous media with a single effective diffusion coefficient that is varied until the computed concentration profile matches the averaged μXRF-determined concentration profiles from the experiment. Values of D_e calculated from the experimental data using the analytical solution from equation (5) were used to calculate the initial tortuosity of the basalt from equation (2).

[19] A pore network was created by defining a 3-D model grid (250 × 250 × 250) with the same resolution as the CT data (4.4 μm) for both the weathered and unweathered samples. A block of CT data in the unweathered basalt was then segmented into porosity (CT value less than 45) and matrix minerals (CT value greater than 45). Each voxel
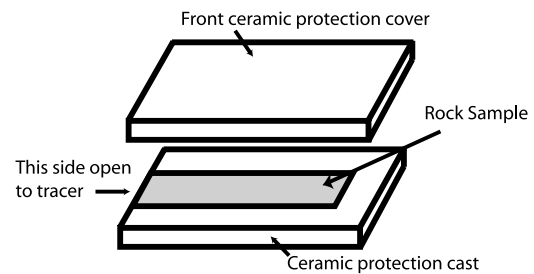
Figure 4. Schematic drawing of the setup for the diffusion experiments. Grey material represents the rock sample surrounded on all but one side by ceramic. The uncovered side is exposed to 0.5 M KBr solution. The sample holder was designed with a removable cover to allow the sample to be analyzed for Br concentrations by μXRF.
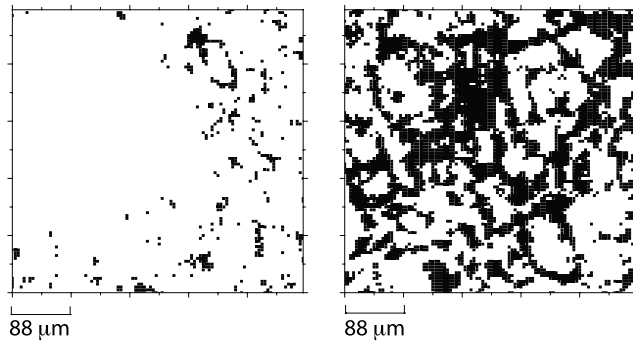
Figure 5. Graphical representation of the grid used in numerical diffusion experiments defined from samples with 5 and 40% total porosity on the left and right, respectively. Black represents voxels defined as pores in which tortuosity was assigned a value equal to 1. White represents voxels defined as minerals in which the tortuosity was assigned a value equal to 1.2×10^{-5}. A value of 45 for CT numbers was used to determine the nature of each voxel (see section 3.1 for further discussion).

was assigned a value representing the tortuosity of the material. Pore space was assigned a tortuosity of one (representing diffusion in water), while the tortuosity of mineral matrix was set equal to the initial tortuosity determined from the 1-D simulation of the bromide tracer experiments in unweathered basalt (Figure 5). In the 3-D simulations a tortuosity (or equivalently, effective diffusivity) for matrix in the pore network was necessary to account for microporosity in these voxels that cannot be resolved with the CT data. A fixed concentration boundary condition for the tracer was used at x = 0, that is, along one side of the cube. The tracer was allowed to numerically diffuse through the pore network. An upscaled, effective diffusion coefficient was calculated from the laterally averaged tracer concentration profile at 7 days (5.904×10^5 s) from the numerical results using the μCT data. These numerical results were then compared to the results from the physical diffusion experiments DP5u and DP5w where a XRF scan was carried out after the same elapsed time. Using the same modeling approach, additional numerical diffusion experiments were performed on smaller blocks of data (550 μm on a side) that were positioned to cross the weathering interface. With this approach, it was possible to analyze the change in effective diffusion coefficient as a function of connected porosity and scale of observation.

4. Results

4.1. Chemical Profiles Across the Core-Rind Transition

[20] Na, K, Ca, Mg, Al, and Si analyzed by EMP show relatively constant concentrations in the core, decreases in concentrations across the 2 mm wide reaction fronts that define the core-rind transition, and relatively constant concentrations in the rind. In contrast, concentrations of Fe and Ti generally increase from core to rind (Table 1). This increase, and a decrease in density from the core to rind, is a result of the removal of other elements during isovolumetric weathering [Sak et al., 2004]. In a system like the

basalt clasts where weathering is isovolumetric [Sak et al., 2004] we can compare the fraction of mass lost or the relative gain of elements ($\tau_{I,j}$) using equation (6),

$$\tau_{i,j} = \left(c_{i,w} c_{j,p} / c_{i,p} c_{j,w} \right) - 1, \qquad (6)$$

where c is the concentration of an immobile element (i) or the element of interest (j) in the parent (p) or weathered (w) material [Brimhall and Dietrich, 1987; Anderson et al., 2002]. In the basalt clasts, Ti has been shown to be relatively immobile [Sak et al., 2004] and can therefore be used to calculate $\tau_{Ti,Ca}$ and $\tau_{Ti,Mg}$ across the reaction front. Negative and positive $\tau_{I,j}$ values represent depletion and enrichment, respectively, of an element relative to parent concentrations. The $\tau_{i,j}$ values of 0 and -1 represent parent concentrations and complete loss of an element, respectively. Figure 6 documents a complete depletion of Ca and Mg across the reaction front. The only minerals in the parent basalt that contain Ca are plagioclase and augite and the only mineral that contains Mg is augite [Sak et al., 2004]. Therefore, the depletion of Ca and Mg indicates complete weathering of plagioclase and augite over a distance of ~1.5 mm.

4.2. Quantification of Total Porosity and Pore Connectivity

[21] Porosity calculated from the μCT data increases across the reaction front from ~3% in the core to ~40% in the rind using a threshold gray-scale value of 45 (Figure 6). Pore connectivity increases with increasing total porosity (Figure 7). At low ϕ_T (<15%), ϕ_e (defined by equation (4) using the code Percolate [Bentz et al., 2002] on the 3-D data) is <1%. The connectivity increases to 100% as ϕ_T changes over a range from 18–25%. At ϕ_T higher than ~25% ϕ_e approaches ϕ_T (Figure 8). The range over which ϕ_e increases from 0 to ϕ_T increases with the size of the sample (Figure 8). Images rendered from the μCT data are provided in the auxiliary material.

4.3. Laboratory Tracer Diffusion Experiments and Pore Network Modeling

[22] Effective diffusion coefficients were calculated from μXRF concentration profiles averaged over the three laboratory tracer experiments on different samples. These coefficients equaled 1.75×10^{-10} cm^2 s^{-1} for unweathered and 2.4×10^{-9} cm^2 s^{-1} for weathered basalt (Tables 2a and 2b). The initial tortuosity value of the unweathered basalt is calculated to be 1.2×10^{-5} on the basis of equation (2). Therefore, in all 3-D pore network simulations of diffusion, voxels defined as matrix minerals (CT value greater than 45) were assigned the tortuosity of the unweathered basalt (1.2×10^{-5}) and voxels defined as porosity (CT value less than or equal to 45) were assigned a tortuosity of 1. To carry out the 3-D simulations, a 1.33 mm^3 pore network (1.1 mm on a side) was imported into the code CrunchFlow, with grid dimensions corresponding exactly to the voxel size of 4.4 microns on a side. Effective diffusion coefficients determined from model results after 7 days from an average concentration profile in the direction of diffusion are 1.2×10^{-10} cm^2 s^{-1} and 1.0×10^{-8} cm^2 s^{-1} for the unweathered and weathered basalt, respectively.

Table 1. Average Elemental Weight Percent and τ Values From 10 Profiles Across the Weathering Interface of Two Basalt Clasts

Distance From Outer Surface (mm)	K	Na	Ca	Mg	Fe	Al	Si	Ti	$\tau_{K,Ti}$	$\tau_{Na,Ti}$	$\tau_{Ca,Ti}$	$\tau_{Mg,Ti}$	$\tau_{Fe,Ti}$	$\tau_{Al,Ti}$	$\tau_{Si,Ti}$
27.00	0.13	0.05	0.17	0.13	11.18	14.60	5.60	0.71	−0.88	−0.99	−0.99	−0.96	0.08	−0.45	−0.93
27.05	0.09	0.05	0.16	0.08	10.18	15.16	4.31	0.51	−0.89	−0.98	−0.98	−0.96	0.35	−0.24	−0.93
27.10	0.10	0.05	0.18	0.08	9.40	15.38	6.11	0.55	−0.87	−0.98	−0.98	−0.96	0.16	−0.27	−0.90
27.15	0.11	0.05	0.17	0.10	8.81	15.08	5.89	0.44	−0.84	−0.98	−0.98	−0.95	0.35	0.04	−0.89
27.20	0.11	0.05	0.20	0.10	9.92	13.06	5.30	0.55	−0.87	−0.98	−0.98	−0.96	0.27	−0.25	−0.92
27.25	0.13	0.05	0.17	0.09	9.65	15.74	5.20	0.51	−0.83	−0.98	−0.98	−0.96	0.31	−0.13	−0.91
27.30	0.10	0.05	0.21	0.10	10.67	13.13	5.13	0.56	−0.89	−0.98	−0.98	−0.96	0.27	−0.39	−0.92
27.35	0.12	0.06	0.26	0.10	10.87	10.22	6.02	0.52	−0.87	−0.98	−0.98	−0.96	0.45	−0.36	−0.91
27.40	0.12	0.06	0.23	0.12	12.70	11.13	6.33	0.79	−0.91	−0.99	−0.99	−0.96	0.08	−0.62	−0.94
27.45	0.13	0.06	0.23	0.12	10.83	14.40	5.47	0.58	−0.85	−0.98	−0.98	−0.95	0.28	−0.35	−0.92
27.50	0.12	0.06	0.17	0.11	9.89	14.84	5.23	0.55	−0.87	−0.98	−0.99	−0.95	0.22	−0.26	−0.92
27.55	0.11	0.05	0.14	0.10	9.63	15.26	5.78	0.45	−0.86	−0.98	−0.99	−0.95	0.45	−0.01	−0.90
27.60	0.17	0.07	0.24	0.12	8.88	15.25	6.28	0.43	−0.80	−0.98	−0.97	−0.94	0.41	0.10	−0.90
27.65	0.12	0.06	0.22	0.12	8.26	13.85	6.41	0.34	−0.81	−0.97	−0.96	−0.92	0.70	0.21	−0.85
27.70	0.18	0.07	0.23	0.11	8.59	12.39	6.74	0.45	−0.79	−0.98	−0.97	−0.94	0.29	−0.27	−0.89
27.75	0.23	0.07	0.19	0.17	10.88	10.11	7.31	0.48	−0.74	−0.98	−0.98	−0.92	0.53	−0.48	−0.88
27.80	0.17	0.08	0.22	0.22	12.93	10.07	7.33	0.56	−0.82	−0.98	−0.98	−0.91	0.55	−0.54	−0.89
27.85	0.18	0.08	0.42	0.27	12.97	9.89	7.89	0.59	−0.84	−0.98	−0.95	−0.89	0.53	−0.45	−0.88
27.90	0.16	0.10	0.20	0.27	13.96	8.33	7.37	0.72	−0.87	−0.98	−0.99	−0.91	0.32	−0.66	−0.91
27.95	0.16	0.10	0.24	0.28	14.76	8.56	7.65	0.66	−0.85	−0.98	−0.98	−0.90	0.53	−0.66	−0.90
28.00	0.15	0.09	0.21	0.35	13.69	8.49	7.38	0.58	−0.85	−0.97	−0.99	−0.86	0.59	−0.59	−0.90
28.05	0.15	0.11	0.26	0.42	13.13	8.37	8.53	0.63	−0.85	−0.97	−0.98	−0.84	0.41	−0.63	−0.89
28.10	0.15	0.11	0.23	0.49	12.02	10.54	7.73	0.49	−0.82	−0.96	−0.98	−0.78	0.64	−0.29	−0.87
28.15	0.11	0.10	0.28	0.48	11.95	9.50	7.96	0.54	−0.87	−0.97	−0.98	−0.80	0.52	−0.40	−0.87
28.20	0.16	0.14	0.23	0.43	13.00	8.18	8.85	0.50	−0.79	−0.95	−0.98	−0.81	0.76	−0.45	−0.86
28.25	0.26	0.16	0.22	0.35	13.49	9.18	8.90	0.61	−0.74	−0.96	−0.98	−0.87	0.50	−0.57	−0.88
28.30	0.28	0.16	0.23	0.23	13.16	9.59	8.45	0.54	−0.71	−0.94	−0.98	−0.91	0.67	−0.35	−0.88
28.35	0.37	0.22	0.28	0.28	12.04	9.17	9.71	0.58	−0.62	−0.94	−0.98	−0.89	0.41	−0.53	−0.86
28.40	0.41	0.26	0.32	0.35	11.26	7.62	11.52	0.63	−0.62	−0.93	−0.98	−0.88	0.22	−0.63	−0.86
28.45	0.45	0.38	0.38	0.32	9.81	6.57	13.63	0.62	−0.56	−0.90	−0.97	−0.88	0.09	−0.68	−0.83
28.50	0.41	0.39	0.40	0.30	10.42	6.27	13.19	0.66	−0.61	−0.90	−0.97	−0.90	0.07	−0.74	−0.84
28.55	0.34	0.36	0.46	0.32	10.21	6.70	10.21	0.62	−0.63	−0.88	−0.96	−0.89	0.24	−0.67	−0.85
28.60	0.38	0.49	0.56	0.41	11.35	7.78	11.90	0.57	−0.53	−0.83	−0.95	−0.84	0.40	−0.61	−0.81
28.65	0.38	0.53	0.64	0.32	10.66	6.81	12.44	0.54	−0.51	−0.81	−0.94	−0.86	0.38	−0.64	−0.79
28.70	0.37	0.56	0.73	0.38	10.13	6.22	13.22	0.58	−0.59	−0.84	−0.94	−0.85	0.17	−0.73	−0.81
28.75	0.40	0.68	0.98	0.51	10.16	6.19	15.53	0.60	−0.55	−0.81	−0.92	−0.79	0.14	−0.74	−0.78
28.80	0.49	0.85	1.32	0.79	9.73	6.33	18.30	0.58	−0.44	−0.76	−0.89	−0.68	0.13	−0.72	−0.73
28.85	0.51	1.07	1.69	0.87	8.85	6.86	20.80	0.53	−0.25	−0.61	−0.81	−0.59	0.24	−0.60	−0.60
28.90	0.59	1.36	2.62	1.03	8.45	8.17	25.17	0.47	−0.17	−0.52	−0.71	−0.49	0.24	−0.55	−0.53
28.95	0.70	1.53	3.61	1.35	7.95	9.13	30.35	0.47	0.04	−0.43	−0.58	−0.32	0.19	−0.48	−0.40
29.00	0.65	1.78	4.20	1.59	7.28	10.36	33.86	0.46	−0.03	−0.35	−0.52	−0.21	0.07	−0.44	−0.35
29.05	0.59	1.93	5.13	1.83	7.38	11.07	36.04	0.48	−0.18	−0.34	−0.43	−0.15	0.03	−0.43	−0.34
29.10	0.59	1.99	5.71	2.10	8.44	11.10	37.42	0.60	−0.31	−0.43	−0.50	−0.16	−0.03	−0.53	−0.44
29.15	0.58	2.07	5.99	2.03	7.87	12.08	38.87	0.52	−0.25	−0.32	−0.37	−0.10	0.03	−0.40	−0.33
29.20	0.54	2.03	6.28	2.10	7.25	12.49	39.15	0.46	−0.20	−0.23	−0.22	0.07	0.08	−0.27	−0.22
29.25	0.51	2.09	6.28	1.97	6.83	12.94	39.20	0.39	−0.10	−0.06	−0.10	0.16	0.19	−0.08	−0.09
29.30	0.49	2.21	6.45	1.79	6.38	13.69	39.82	0.35	0.02	0.11	0.04	0.19	0.23	0.08	0.06
29.35	0.63	2.41	6.33	1.21	5.88	14.35	40.21	0.45	−0.05	−0.09	−0.26	−0.37	−0.10	−0.16	−0.20
29.40	0.51	2.33	7.20	1.57	5.66	13.96	40.13	0.38	−0.07	0.07	0.05	−0.05	0.01	0.02	−0.03
29.45	0.51	2.34	6.71	1.81	6.69	13.04	39.99	0.51	−0.32	−0.23	−0.30	−0.19	−0.12	−0.32	−0.30
29.50	0.63	2.32	6.46	2.00	6.25	12.69	40.77	0.36	0.31	0.28	0.20	0.28	0.19	0.22	0.19
29.55	0.68	2.37	5.63	2.21	7.77	11.65	40.56	0.54	−0.01	−0.15	−0.28	−0.03	0.01	−0.27	−0.21
29.60	0.67	2.30	6.22	2.41	7.55	12.01	40.66	0.52	−0.12	−0.24	−0.32	0.06	−0.02	−0.36	−0.29
29.65	0.61	2.20	6.28	2.18	7.16	12.37	40.41	0.52	−0.22	−0.29	−0.35	−0.02	−0.07	−0.37	−0.31
29.70	0.54	2.01	6.46	2.34	7.19	12.56	39.77	0.51	−0.28	−0.33	−0.34	0.07	−0.05	−0.36	−0.31
29.75	0.50	1.97	6.70	2.14	6.69	12.99	39.51	0.41	−0.19	−0.19	−0.13	0.19	0.09	−0.18	−0.15
29.80	0.46	2.08	7.35	1.60	4.84	14.63	39.91	0.30	0.07	0.27	0.44	0.25	0.12	0.40	0.26
29.85	0.53	2.12	6.71	1.56	5.14	14.48	40.48	0.32	0.13	0.14	0.14	0.13	0.09	0.19	0.13
29.90	0.42	2.00	6.75	1.94	6.23	13.59	39.45	0.37	−0.20	−0.03	−0.02	0.34	0.20	−0.04	0.00
29.95	0.42	2.16	6.69	1.71	5.65	14.23	40.36	0.26	0.18	0.45	0.41	0.53	0.49	0.45	0.41
30.00	0.48	2.31	6.76	1.80	5.38	13.96	41.12	0.32	0.00	0.21	0.07	0.38	0.15	0.09	0.12
30.05	0.57	2.32	6.85	1.84	5.19	13.36	42.03	0.33	0.17	0.19	0.06	0.36	0.10	0.04	0.13
30.10	0.52	2.30	6.69	1.89	6.37	13.06	41.14	0.48	−0.26	−0.20	−0.28	−0.09	−0.10	−0.30	−0.25
30.15	0.69	2.19	6.85	1.91	6.11	12.55	41.87	0.45	0.04	−0.17	−0.21	−0.01	−0.07	−0.29	−0.18
30.20	0.67	2.28	7.02	1.32	4.77	15.43	41.80	0.36	0.26	0.06	−0.01	−0.18	−0.12	0.09	0.02
30.25	0.50	2.28	7.18	1.21	4.65	15.03	40.89	0.36	0.07	0.25	0.16	−0.13	−0.07	0.20	0.16
30.30	0.50	1.97	7.34	1.47	4.86	14.68	40.47	0.32	0.23	0.28	0.42	0.21	0.11	0.41	0.36
30.35	0.68	1.96	7.62	1.32	4.83	15.18	40.65	0.38	0.23	−0.13	0.01	−0.23	−0.17	−0.01	−0.05
30.40	0.65	2.15	7.62	1.24	4.28	15.34	41.03	0.32	0.51	0.21	0.30	0.01	−0.04	0.29	0.23
30.45	0.62	2.19	7.40	1.40	4.58	14.77	41.75	0.32	0.35	0.20	0.21	0.02	−0.02	0.20	0.19
30.50	0.52	1.89	7.59	1.86	5.95	13.97	40.66	0.40	−0.09	−0.14	0.02	0.11	0.03	−0.07	−0.03
30.55	0.50	2.01	7.81	1.28	4.75	15.89	40.58	0.32	0.05	0.06	0.21	−0.07	0.00	0.24	0.10

Table 1. (continued)

Distance From Outer Surface (mm)	Weight Percent Element														
	K	Na	Ca	Mg	Fe	Al	Si	Ti	$\tau_{K,Ti}$	$\tau_{Na,Ti}$	$\tau_{Ca,Ti}$	$\tau_{Mg,Ti}$	$\tau_{Fe,Ti}$	$\tau_{Al,Ti}$	$\tau_{Si,Ti}$
30.60	0.53	2.13	7.82	0.93	3.71	16.85	40.76	0.22	0.69	0.68	0.82	−0.04	0.12	0.98	0.65
30.65	0.50	2.07	7.55	1.35	5.15	15.38	40.55	0.38	−0.05	−0.03	0.06	−0.11	−0.04	0.07	0.00
30.70	0.57	1.92	7.17	1.93	6.53	13.69	40.17	0.48	0.04	−0.15	−0.09	−0.09	−0.05	−0.12	−0.09
30.75	0.54	2.14	7.17	1.75	5.81	14.13	40.89	0.37	−0.02	−0.02	−0.03	0.07	0.05	−0.06	−0.02
30.80	0.50	2.18	7.14	1.58	5.59	14.48	40.89	0.39	−0.13	−0.06	−0.09	−0.08	−0.04	−0.09	−0.08
30.85	0.50	2.28	7.09	1.57	5.38	14.43	41.60	0.39	−0.09	0.04	−0.04	0.06	−0.01	−0.03	−0.01
30.90	0.59	2.26	6.65	1.74	5.77	13.97	41.73	0.38	0.07	0.01	−0.11	0.02	0.03	−0.09	−0.03
30.95	0.47	1.98	6.49	1.84	5.23	12.40	38.40	0.31	0.06	0.16	0.14	0.42	0.10	0.08	0.17
Average Parent[a]	0.53	2.12	7.14	1.58	5.40	14.42	40.62	0.37							

[a]Average value from last eight data points.

[23] An additional 3-D simulation was carried out with a 0.166 mm^3 pore network defined by CT data from the unweathered basalt. D_e values are 3.7×10^{-11} cm^2 s^{-1} and 1.2×10^{-10} cm^2 s^{-1} for the 0.166 and 1.38 mm^3 samples, respectively. Numerical diffusion experiments using 0.166 mm^3 pore networks defined by CT data across the weathering interface demonstrate that the calculated effective diffusion coefficient increases with connected porosity as expected (Tables 2a and 2b and Figure 9). Note that the upscaled effective diffusion coefficients determined from the pore network modeling agree closely with the experimentally determined values.

5. Discussion

5.1. Pore Connectivity

[24] If we assume that all changes in porosity are the result of weathering of the parent basalt, the μCT data allows us to examine how changes in effective or connected porosity are related to changes in total porosity induced by weathering (Figure 6). Effective porosity in the parent basalt is 0% at the resolution of the CT data and remains 0% until total porosity increases to $\sim$9%.

[25] Percolation theory predicts a critical porosity below which connected pathways from one end of the system to the other are not available [Sahimi, 1994]. Percolation theory is typically used to describe the degree of connectivity of disordered media [Scher and Zallen, 1970]. A variable (p) is defined to range from 0 to 1 such that when $p = 0$, all pathways are discontinuous across the sample interval and where $p = 1$ all pathways are continuous [Sahimi, 1994]. A percolation threshold (p_c) exists for each sample such that when $p < p_c$ there are no complete connected pathways from one edge of the material to the other, but at p_c one fully connected pathway exists. As defined, the value of p_c is constant if the sample size is larger than the representative elementary volume (REV). In sample sizes smaller than the REV, p_c is scale dependent and can vary with sample interval size in heterogeneous media such as rocks [Sahimi, 1994]. When $p \geq p_c$ there
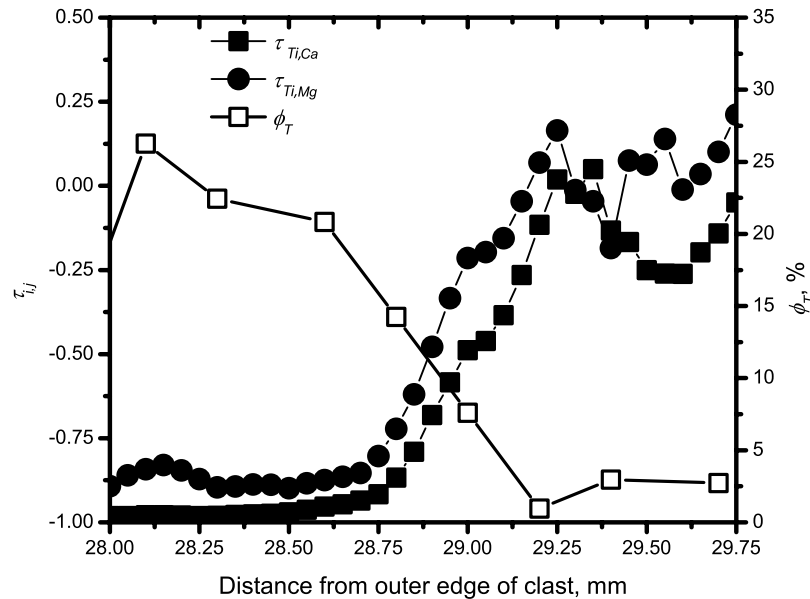

Figure 6. Values of $\tau_{i,j}$ for Ca and Mg and total porosity plotted versus distance from the outer edge of the basalt clasts from the 125 ka terrace. For clasts from the 125 ka terrace the weathering interface is generally located between 28.6 and 29.1 mm from the outer edge of the basalt clast. Here $\tau_{i,j}$ values for Ca and Mg decrease across the weathering front, consistent with weathering of plagioclase and augite. There is a corresponding increase in total porosity associated with weathering.
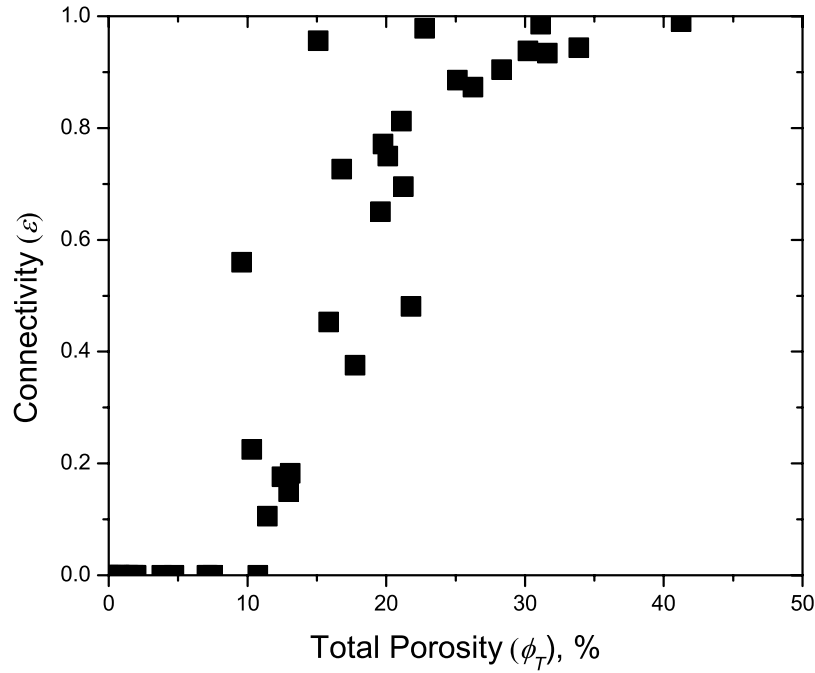
Figure 7. A plot of the connectivity versus the total porosity calculated for sets of CT data measured on 0.166 mm^3 volumes along transects across the core-rind interface in the same basalt clast portrayed in Figure 2. Measured values of connectivity (ε) increase with increasing total porosity once a critical porosity (ϕ_c, 9%) is reached.
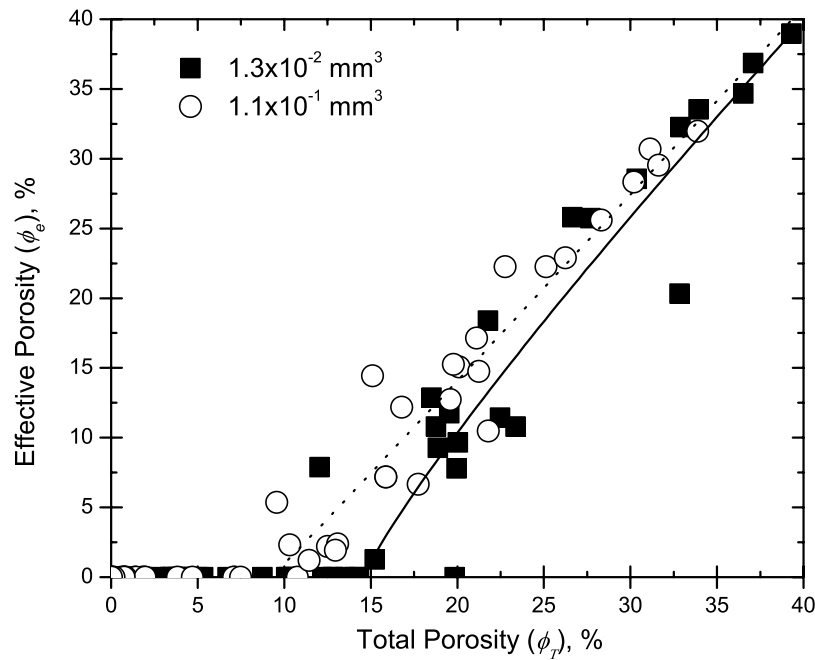
Figure 8. Effective porosity plotted versus total porosity as calculated for volume elements of 1.33×10^{-3} or 1.06×10^{-2} mm^3 using CT (resolution of 4.4 μm). Symbols represent measured values at points positioned along a transect across the core-rind interface (see text and Figure 7). Critical porosity is determined by fitting the data to equation (7) and critical porosity values are $14 \pm 2\%$ for a sample size of 1.33×10^{-3} mm^3 (fit shown by solid line) and $9 \pm 1\%$ for a sample size of 1.06×10^{-2} mm^3 (fit shown by dotted line).

Table 2a. Results From Physical Diffusion Experiments

Sample	Time (hours)	Distance to Br Front (μm)	D_e (cm^2 s^{-1})	Percent Porosity
DP3	804	225	2.31×10^{-10}	3
DP3	403	82	1.94×10^{-10}	3
DP6	813	248	1.92×10^{-10}	3
DP6	402.5	160	5.09×10^{-11}	3
DP5u	164	105	2.05×10^{-10}	3
DP5w	164	360	2.41×10^{-9}	~14

remains at least one fully connected pathway across the sample and when applied to fluid transport through porous media, p_c becomes the critical porosity (ϕ_c) [*Dasgupta et al.*, 2000].

[26] We can estimate a critical porosity for the basalt sample by fitting the nonzero effective porosity (obtained by using Percolate) versus total porosity (from CT scans) data reported in Figure 8 to a scaling law on the basis of percolation theory [*Stauffer*, 1985; *Ellis and Wright*, 2006] (equation (7))

$$\phi_e = a(\phi_T - \phi_c)^\beta, \qquad (7)$$

where a is a preexponential factor and β is the scaling exponent [*Stauffer*, 1985]. We note here that equation (7) is valid for $\phi_T > \phi_C$. Values of a are 2.4 and 1.3 and values of β are 0.9 and 1.0 for samples 110 and 220 μm on a side, respectively. The critical porosity values using this method are 14 ± 2% and 9 ± 1% for the samples that are 110 and 220 μm on a side, respectively. The critical porosity value decreases with increasing sample size at the scales we were able to measure. Due to the narrow width of the weathering interface we are unable to sample larger volumes of data to assess whether these sample sizes are greater than or equal to the size of a representative elementary volume at which the critical porosity value determined would be representative of the bulk material. Therefore, the lower of the two critical porosity values ($\phi_c = 9\%$) is our best estimate of the critical porosity above which some pores are connected in the weathering basalt clast.

[27] In bulk rocks, the value of ϕ_c can vary as a function of pore size, shape and orientation [e.g., *Ewing and Gupta*, 1993]. In the sample studied here the dissolution of plagioclase is the first reaction to result in the creation of secondary porosity. The pores that result from the dissolution of plagioclase are the same size and shape as the original plagioclase grains (Figure 1). Therefore, the pore size, shape and orientation of the secondary porosity, and thus the value of the critical porosity, are a function of the size, shape and orientation of the parent plagioclase grains. This also implies that crystalline rocks with distinct textures that undergo chemical weathering may show differing critical porosities.

[28] Reported critical porosities in other geological materials vary on the basis of lithology and the presence or absence of fractures. *Kieffer et al.* [1999] measured total and effective porosity for Fontainebleau sandstone and reported a critical porosity of <5%. Connected porosity has been identified in basalts, limestone, granodiorite, and sandstone where total porosity is as low as 1% [*Tugrul*, 2004]. Such variations in critical porosity values have been attributed to the presence of microcracks that provide direct conduits for

fluid transport even in low-porosity systems [*Gueguen et al.*, 1997; *Tullborg and Larson*, 2006]. Methods used to measure both total and effective porosity also vary and may cause method-specific variations in critical porosity values. For example, *Tugrul* [2004] reports effective porosity values of 1.2% in unaltered basalt and 3.5% in unaltered granodiorite on the basis of mercury intrusion techniques. In contrast, *Tullborg and Larson* [2006] calculated a total porosity of 0.89 to 1.52% in unaltered quartz monzodiorite using the same methods as *Tugrul* [2004] but an effective porosity of 0.38 to 0.57%, depending on sample size, using water saturation methods. Comparing results between these two studies is difficult because Hg intrusion has been shown to overestimate effective porosity relative to measurement by water saturation [*Sato et al.*, 1997].

[29] The approximate value of critical porosity we observe for this sample is within the range of values predicted by percolation theory. Theoretical calculations and model estimates of the critical porosity in porous diffusive systems vary from 8 to 18% [*Scher and Zallen*, 1970; *Tarafdar and Roy*, 1998; *Dasgupta et al.*, 2000; *Cheadle et al.*, 2004] while experimental measurement of permeability in rocks as a function of porosity suggest a range of critical porosities ranging from 3 to 10% [*Du Plessis*, 1999; *van der Marck*, 1999]. The lower value of the critical porosity associated with these experimental studies may reflect the fact that natural samples are not strictly disordered. While a few studies have incorporated changes in effective porosity and transport parameters as a function of weathering or water-rock interaction [*Steefel and Lasaga*, 1994; *Steefel and Lichtner*, 1998; *Saripalli et al.*, 2001], experimental studies of these effects are lacking.

[30] Below the critical porosity, transport properties should not be greatly influenced by changes in total porosity. However, continuum models of chemical weathering or water-rock interaction are generally used to predict weathering at the field scale and typically only provide information on changes in total porosity due to mineral reaction. Equation (7) also provides a useful description of the effective diffusivity for the weathered basalt clast as a function of total porosity above and close to the critical porosity (~9–44%). Below the critical porosity the effective porosity is 0% and above a total porosity of 44% the effective porosity equals the total porosity. Using equation (7), effective diffusion coefficients near the critical porosity can then be estimated from a measure of the effective porosity for use in continuum models of basalt weathering rind formation where the porosity is changing as a result of weathering.

Table 2b. Results From 3-D Diffusion Pore Network Experiments

Sample Size (mm^3)	Time (hours)	Distance to Tracer Front (μm)	D_e (cm^2 s^{-1})	Percent Porosity
1.38	168	83	1.2×10^{-10}	3
1.38	168	776	1.0×10^{-8}	14
0.17	12	12	3.7×10^{-11}	2
0.17	2.4	11.5	1.7×10^{-8}	10
0.17	1.2	16	6.1×10^{-8}	14
0.17	1.2	122	1.9×10^{-7}	21
0.17	0.24	195	4.8×10^{-7}	30
0.17	0.24	236	7.1×10^{-7}	33
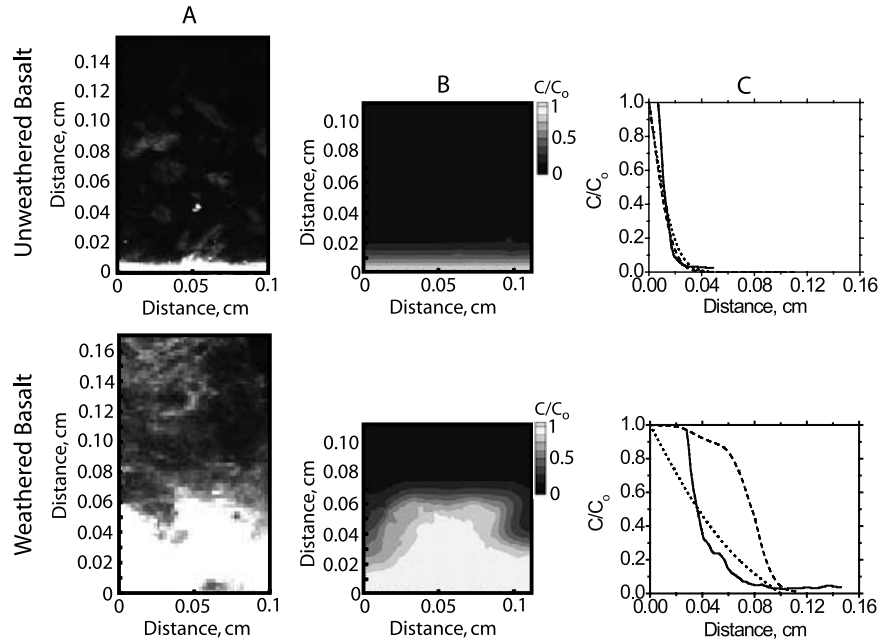
Figure 9. Comparison of results from diffusion experiments and models for (top) unweathered and (bottom) weathered basalt. (a) The μXRF image of Br concentrations measured at the surface of basalt samples in laboratory diffusion experiments after 7 days (see section 2.3). High Br concentrations near the $y = 0$ cm axis are white. (b) Contour plot of Br concentrations from 3-D diffusion simulations run for 7 days at the same scale as μXRF images. The position of the tracer front along the y axis in the models is similar to the position of the Br front in the laboratory diffusion experiments. (c) A plot of concentration of tracer relative to the original tracer concentration (C/C_o) versus distance (cm) measured in laboratory diffusion experiments (solid line) and modeled in 1-D (dotted line) and 3-D (dashed line) numerical models.

5.2. Numerical Diffusion Experiments

[31] The best fit values of D_e determined from 1-D diffusion models are 1.9×10^{-10} cm^2 s^{-1} for the unweathered basalt where porosity equals 3% and 2.5×10^{-9} cm^2 s^{-1} for the weathered basalt where the porosity equals 14%. Concentration profiles from the experiment and the 1-D and 3-D models show good agreement for both weathered and unweathered samples (Figure 9). Values of D_e from 3-D models are in close agreement with the experimentally determined D_e in the unweathered basalt. In the weathered basalt, the value of D_e from the 1-D model is similar to the experimentally determined D_e. However, the D_e determined from the 3-D model is 0.65 orders of magnitude (a factor of 4) faster. A value of D_e that is slower, i.e., more similar to the model-calculated value, is expected due to the fact that the CT data does not include microporosity that contributes to diffusion in the laboratory experiments, but this discrepancy may also be due to the fact the laboratory and numerical experiments were not carried out on the same sample. The heterogeneity of the weathered material is consistent with values of D_e that range from 6.7×10^{-9} cm^2 s^{-1} to 1.1×10^{-8} cm^2 s^{-1}, calculated from concentration profiles measured at different positions using data from the 3-D pore network simulations.

[32] The connectivity of the larger CT-defined pore network in the unweathered basalt is higher than those calculated for the smaller data sets. Correspondingly, a higher D_e value is determined from the larger 3-D pore network models, 3.7×10^{-11} cm^2 s^{-1} for 0.17 mm^3 compared to 1.25×10^{-10} cm^2 s^{-1} for 1.38 mm^3, indicating that there may be a scale dependence to the 3-D modeled values of D_e plotted in Figure 10.

5.3. Total Versus Effective Porosity as a Scaling Parameter in Archie's Law

[33] We have calculated values of D_e using total porosity as the scaling parameter in Archie's law (equation (3)) with a cementation exponent of 2 for comparison to laboratory measured and modeled values of D_e for the weathered basalt (Figure 10). We find that over the range of total porosity studied here scaling effective diffusion coefficients using total porosity over predicts measured and modeled values of D_e. We also calculate D_e using effective porosity as the scaling parameter in Archie's law. For total porosity above and close to the critical porosity (9–44%) equation (7) is used to estimate the effective porosity. equation (3) is then used to calculate D_e in the total porosity range from 9 to 44% using effective porosity as the scaling parameter with a cementation exponent of 2. Above ϕ_T of 44%, ϕ_e equals ϕ_T and the scaled D_e value is the same when either total or effective porosity is used as the scaling parameter. At the resolution of our measurements, ϕ_e below the critical porosity (9%) is 0% suggesting zero diffusivity in the unweathered basalt. However, connectivity values are likely underestimated in the low total porosity range of this sample due to the resolution of the CT data and the small volumes sampled. Pores with a diameter less than 4.4 microns are not included in the CT data and it is likely that values of
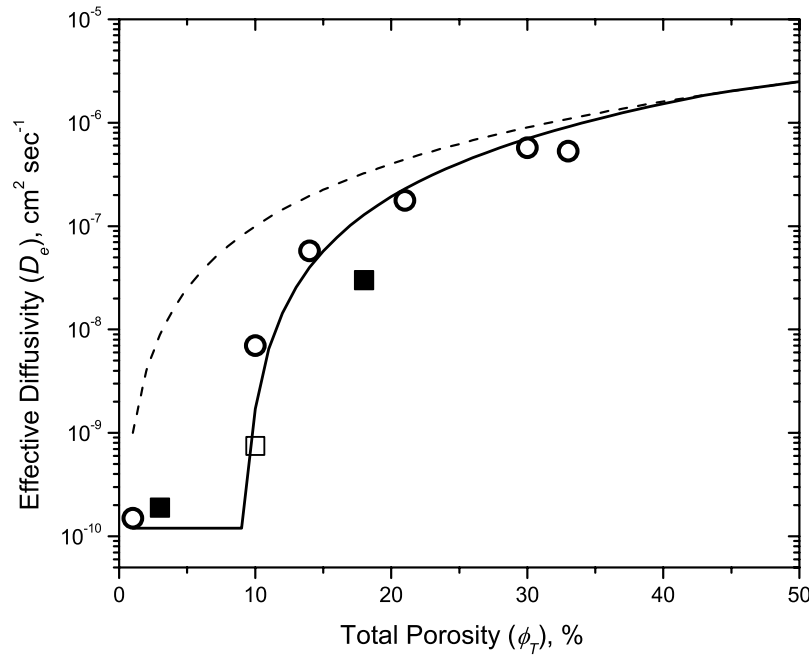
Figure 10. Values of D_e estimated from equation (3) using Archie's law with total porosity (dashed line) or from equation (8) using effective porosity as the scaling parameter (solid line). These estimates are compared with measured D_e in basalt (solid squares for diffusion experiments in this study and open squares for data from *Sato et al.* [1997]). Values of D_e calculated from numerical diffusion experiments are plotted as open circles. At porosities near and below the critical porosity, effective porosity is a better predictor of D_e than total porosity.

connected porosity calculated for samples with very low total porosity are greater than zero. Additionally, results from analysis of a 2.38 mm^3 sample of CT data in the unweathered basalt suggest an effective porosity value of approximately 0.003 %. In fact, an effective diffusion coefficient of 1.75×10^{-10} cm^2 s^{-1} was measured in the unweathered basalt in laboratory experiments. If we assume this effective diffusion coefficient in the unweathered parent basalt (D_p) is representative of the diffusivity at all total porosity values below the critical porosity we can use equation (8) to calculate D_e using effective porosity as a scaling parameter

$$D_e = D_p + D_o(\phi_e)^2. \qquad (8)$$

Using equation (8) to calculate D_e yields values similar to values measured in this basalt clast (Figure 10). These values are also similar to values previously reported for D_e for basalt with 10% effective porosity (7.5×10^{-10} cm^2 s^{-1} [*Sato et al.*, 1997]). Combining equations (7) and (8) provides a useful way to calculate effective diffusion coefficients for continuum modeling of this weathering system on the basis of total porosity, a measurable quantity. Strictly speaking, equations (7) and (8) are not universal laws since they are derived from a single weathered basalt sample. However, we hypothesize that these equations will also be applicable to other rocks and subsurface materials that develop similar pore structures as a result of chemical reactions. These include other basaltic or volcanic rocks with similar primary rock textures. The applicability of equations (7) and (8) to other rock types is currently

unknown. However, the mathematical form of equations (7) and (8) may be similar.

6. Conclusions

[34] As basalt weathers and forms a rind of weathered material, secondary porosity is created through the dissolution of primary minerals. In weathered basalt clasts from Costa Rica, the dissolution of plagioclase and augite results in secondary porosity. This increased porosity allows an increase in the transport of aqueous weathering products away from the core/rind interface by diffusion and therefore increases rates of overall chemical reaction. However, in this sample, until a critical porosity of ∼9% is reached, the number of connected pathways available for fluid transport does not increase and therefore diffusive transport should not increase until this critical porosity is obtained. The critical porosity of a sample can vary as a function of the sample size below the representative elementary volume of the bulk material. In this sample porosity increases from ∼3 to 40% as a result of weathering over a very narrow interface (∼1.5 mm). The critical porosity determined from samples of 110 and 220 μm on a side are within error, and the critical porosity is not scale dependent at the scales we are able to sample. The critical porosity is a function of the pore shape and distribution. In this sample plagioclase is the first phase to dissolve and create secondary porosity. Therefore, the pore shape and distribution, and thus the critical porosity, is controlled by the shape and distribution of plagioclase in the parent basalt. Since the volume percent of plagioclase in the Costa Rica basalts (∼66%) is greater than the critical porosity, then the dissolution of plagioclase

can be considered the rate-limiting step in weathering progression. The presence of a critical porosity suggests that effective diffusion coefficients should be estimated from effective (connected) porosity and not total porosity if reactive transport models are to be used to interpret data from this system. Predicted values of effective diffusion coefficients from equation (8) agree with results from diffusion experiments in both unweathered and weathered basalt.

[35] Numerical models of the diffusion experiments in 1-D, assuming a single homogeneous porous media, and 3-D, where a pore network is defined using CT data, are all consistent with the effective diffusion coefficients measured experimentally. The consistency between these models and the experimental results demonstrates that, where CT-defined pore networks can be measured, they can be used not only to interpret diffusion experiments, but also to perform numerical diffusion experiments in place of time-consuming laboratory diffusion experiments.

References

Adler, P. M., C. G. Jacquin, and J. F. Thovert (1992), The formation factor of reconstructed porous media, *Water Resour. Res.*, 28, 1571–1576, doi:10.1029/92WR00059.

Amiotte-Suchet, P., J. Probst, and W. Ludwig (2003), Worldwide distribution of continental rock lithology: Implications for the atmospheric/soil CO_2 uptake by continental weathering and alkalinity river transport to the oceans, *Global Biogeochem. Cycles*, 17(2), 1038, doi:10.1029/2002GB001891.

Anderson, S. P., W. E. Dietrich, and G. H. Brimhall (2002), Weathering profiles, mass-balance analysis, and rates of solute loss: Linkages between weathering and erosion in a small, steep catchment, *Geol. Soc. Am. Bull.*, 114, 1143–1158.

Archie, G. E. (1942), The electrical resistivity log as an aid in determining some reservoir characteristics, *Trans. Am. Inst. Min. Metall. Pet. Eng.*, 146, 54–62.

Bear, J. (1972), *Dynamics of Fluids in Porous Media*, 764 pp., Elsevier, New York.

Bentz, D. P., and E. J. Garboczi (1992), Modeling the leaching of calcium hydroxide from cement paste: Effects of pore space percolation and diffusivity, *Mater. Struct.*, 25, 523–533, doi:10.1007/BF02472448.

Bentz, D. P., et al. (2002), The visible cement data set, *NIST J. Res.*, 107, 137–148.

Boving, T., and P. Grathwohl (2001), Tracer diffusion coefficients in sedimentary rocks: Correlation to porosity and hydraulic conductivity, *J. Contam. Hydrol.*, 53, 85–100, doi:10.1016/S0169-7722(01)00138-3.

Brantley, S. L. (2008), Kinetics of mineral dissolution, in *Kinetics of Water-Rock Interaction*, edited by S. Brantley, J. Kubicki, and A. F. White, pp. 151–210, Springer, New York.

Brimhall, G. H., and W. E. Dietrich (1987), Constitutive mass balance relations between chemical composition, volume, density, porosity, and strain in metasomatic hydrochemical systems: Results on weathering and pedogenesis, *Geochim. Cosmochim. Acta*, 51, 567–587, doi:10.1016/0016-7037(87)90070-6.

Cheadle, M. J., M. T. Elliott, and D. Mckenzie (2004), Percolation threshold and permeability of crystallizing igneous rocks: The importance of textural equilibrium, *Geology*, 32, 757–760, doi:10.1130/G20495.1.

Colman, S., and K. Pierce (1981), *Weathering Rinds on Andesitic and Basaltic Stones as a Quaternary Age Indicator, Western United States*, U. S. Geol. Soc., Reston, Va.

Dasgupta, R., S. Roy, and S. Tarafdar (2000), Correlation between porosity, conductivity and permeability of sedimentary rocks - a ballistic deposition model, *Physica A*, 275, 22–32, doi:10.1016/S0378-4371(99)00388-X.

Dessert, C., B. Dupre, J. Gaillardet, L. Francois, and C. Allegre (2003), Basalt weathering laws and the impact of basalt weathering on the global carbon cycle, *Chem. Geol.*, 202, 257–273, doi:10.1016/j.chemgeo.2002.10.001.

Dullien, F. A. L. (1992), *Porous Media: Fluid Transport and Pore Structure*, 2nd ed., Academic, San Diego, Calif.

Du Plessis, J. P. (1999), Introducing a percolation threshold in pore-scale modeling, *Phys. Chem. Earth A*, 24, 617–623, doi:10.1016/S1464-1895(99)00089-7.

Ellis, S. R., and J. L. Wright (2006), Modeling of aqueous transport in rigid porous matrices near the percolation threshold, *Pharm. Res.*, 23, 2441–2453, doi:10.1007/s11095-006-9073-7.

Ewing, R. P., and S. C. Gupta (1993), Percolation and permeability in partially structured networks, *Water Resour. Res.*, 29, 3179–3188, doi:10.1029/93WR01497.

Fletcher, R. C., H. L. Buss, and S. L. Brantley (2006), A spheroidal weathering model coupling porewater chemistry to soil thicknesses during steady-state denudation, *Earth Planet. Sci. Lett.*, 244, 444–457, doi:10.1016/j.epsl.2006.01.055.

Garboczi, E. J., D. P. Bentz, and N. S. Martys (1999), Digital images and computer modeling, in *Methods in the Physics of Porous Media*, edited by P. Wong, pp. 1–41, Academic, San Diego, Calif.

Gueguen, Y., T. Chelidze, and M. Le Ravalec (1997), Microstructure, percolation thresholds, and rock physical properties, *Tectonophysics*, 279, 23–35, doi:10.1016/S0040-1951(97)00132-7.

Hausrath, E. M., A. K. Navarre-Sitchler, P. B. Sak, C. I. Steefel, and S. L. Brantley (2008), Basalt weathering rates on Earth and the duration of liquid water on the plains of Gusev Crater, Mars, *Geology*, 36, 67–70, doi:10.1130/G24238A.1.

Ketcham, R., and G. Iturrino (2005), Nondestructive high-resolution visualization and measurement of anisotropic effective porosity in complex lithologies using high-resolution X-ray computed tomography, *J. Hydrol.*, 302, 92–106, doi:10.1016/j.jhydrol.2004.06.037.

Kieffer, B., C. Jove, E. Oelkers, and J. Schott (1999), An experimental study of the reactive surface area of the Fontainebleau sandstone as a function of porosity, permeability, and fluid flow rate, *Geochim. Cosmochim. Acta*, 63, 3525–3534, doi:10.1016/S0016-7037(99)00191-X.

Lebedeva, M., R. C. Fletcher, V. Balashov, and S. Brantley (2007), A reactive diffusion model describing transformation of bedrock to saprolite, *Chem. Geol.*, 244, 624–645, doi:10.1016/j.chemgeo.2007.07.008.

Lever, D. A., M. H. Bradbury, and S. J. Hemingway (1985), The effect of dead-end porosity on rock-matrix diffusion, *J. Hydrol.*, 80, 45–76, doi:10.1016/0022-1694(85)90074-5.

Lichtner, P. (1996), Continuum formulation of multicomponent-multiphase reactive transport, in *Reactive Transport in Porous Media*, edited by P. Lichtner et al., pp. 1–82, Mineral. Soc. of Am., Washington, D. C.

Lumb, P. (1983), Engineering properties of fresh and decomposed igneous rocks from Hong Kong, *Eng. Geol.*, 19, 81–94, doi:10.1016/0013-7952(83)90027-3.

Maher, K., C. I. Steefel, D. J. DePaolo, and B. I. Viani (2006), The mineral dissolution rate conundrum: Insights from reactive transport modeling of U isotopes and pore fluid chemistry in marine sediments, *Geochim. Cosmochim. Acta*, 70, 337–363, doi:10.1016/j.gca.2005.09.001.

Millington, R. J., and J. P. Quirk (1964), Formation factor + permeability equations, *Nature*, 202, 143–146, doi:10.1038/202143a0.

Moore, J. (2008), Biogeochemistry of granitic weathering, Ph.D. thesis, Pa. State Univ., University Park, Pa.

Navarre-Sitchler, A. K., and S. L. Brantley (2007), Basalt weathering across scales, *Earth Planet. Sci. Lett.*, 261, 321–334, doi:10.1016/j.epsl.2007.07.010.

Oelkers, E. (1996), Physical and chemical properties of rocks and fluids for chemical mass transport calculations, in *Reactive Transport in Porous Media*, edited by P. Lichtner et al., pp. 335–371, Mineral. Soc. of Am., Washington, D. C.

Oguchi, C. T., and Y. Matsukura (2000), Effect of porosity on the Increase in weathering-rind thickness of andesite gravel, *Eng. Geol.*, 55, 77–89, doi:10.1016/S0013-7952(99)00108-8.

Pelt, E., F. Chabaux, C. Innocent, A. K. Navarre-Sitchler, P. B. Sak, and S. L. Brantley (2009), ^{238}U-^{234}U-^{230}Th chronometry of weathering rinds: Rock alteration rate and paleo-isotopic record of weathering fluid, *Earth Planet. Sci. Lett.*, 276, 98–105.

Sahimi, M. (1994), *Applications of Percolation Theory*, Taylor and Francis, London.

Sak, P. B., D. M. Fisher, T. W. Gardner, K. Murphy, and S. L. Brantley (2004), Rates of weathering rind formation on Costa Rican basalt, *Geochim. Cosmochim. Acta*, *68*, 1453–1472, doi:10.1016/j.gca.2003.09.007.

Saripalli, K. P., P. Meyer, D. Bacon, and V. L. Freedman (2001), Changes in hydrologic properties of aquifer media due to chemical reactions: A review, *Critical Rev. Environ. Sci. Technol.*, *31*, 311–349, doi:10.1080/20016491089244.

Sato, H., T. Shibutani, and M. Yui (1997), Experimental and modelling studies on diffusion of Cs, Ni and Sm in grandodiorite, basalt and mudstone, *J. Contam. Hydrol.*, *26*, 119–133, doi:10.1016/S0169-7722(96)00063-0.

Scher, H., and R. Zallen (1970), Cricital denisty in percolation processes, *J. Chem. Phys.*, *53*, 3759–3761, doi:10.1063/1.1674565.

Shen, L., and Z. Chen (2007), Critical review of hte impact of tortuosiuty on diffusion, *Chem. Eng. Sci.*, *62*, 3748–3755, doi:10.1016/j.ces.2007.03.041.

Sitchler, A. K. (2008), Weathering advance rates in basalt: Prediction and comparison across scales, Ph.D. thesis, Pa. State Univ., University Park, Pa.

Stauffer, D. (1985), *Introduction to Percolation Theory*, Taylor and Francis, London.

Steefel, C. I., and A. C. Lasaga (1994), A coupled model for transport of multiple chemical-species and kinetic precipitation dissolution reactions with application to reactive flow in single-phase hydrothermal systems, *Am. J. Sci.*, *294*, 529–592.

Steefel, C. I., and P. C. Lichtner (1998), Multicomponent reactive transport in discrete fractures: Part I. Controls on reaction front geometry, *J. Hydrol.*, *209*, 186–199, doi:10.1016/S0022-1694(98)00146-2.

Steefel, C. I., D. J. Depaolo, and P. C. Lichtner (2005), Reactive transport modeling: An essential tool and a new research approach for the Earth Sciences, *Earth Planet. Sci. Lett.*, *240*, 539–558, doi:10.1016/j.epsl.2005.09.017.

Tarafdar, S., and S. Roy (1998), A growth model for porous sedimentary rocks, *Physica B*, *254*, 28–36, doi:10.1016/S0921-4526(98)00431-1.

Tugrul, A. (2004), The effect of weathering on pore geometry and compressive strength of selected rock types from Turkey, *Eng. Geol.*, *75*, 215–227, doi:10.1016/j.enggeo.2004.05.008.

Tullborg, E. L., and S. A. Larson (2006), Porosity in crystalline rocks—A matter of scale, *Eng. Geol.*, *84*, 75–83, doi:10.1016/j.enggeo.2005.12.001.

Ullman, W. J., and R. C. Aller (1982), Diffusion coefficients in nearshore marine sediments, *Limnol. Oceanogr.*, *27*, 552–556.

van der Marck, S. C. (1999), Evidence for a nonzero transport threshold in porous media, *Water Resour. Res.*, *35*, 595–599, doi:10.1029/1998WR900062.

Velbel, M. A. (1993), Constancy of silicate-mineral weathering-rate ratios between natural and experimental weathering: Implications for hydrologic control of differences in absolute rates, *Chem. Geol.*, *105*, 89–99, doi:10.1016/0009-2541(93)90120-8.

White, A. (2008), Quantitative approaches to characterizing natural chemical weathering rates, in *Kinetics of Water-Rock Interaction*, edited by S. Brantley, J. Kubicki, and A. F. White, pp. 469–500, Springer, New York.

White, A., and S. Brantley (1995), *Chemical Weathering Rates of Silicate Minerals*, Mineral. Soc. of Am., Washington, D. C.

————————————

S. L. Brantley, Center for Environmental Kinetics Analysis, Pennsylvania State University, University Park, PA 16802, USA.

A. Navarre-Sitchler, Department of Geology and Geophysics, University of Wyoming, Laramie, WY 82071, USA. (alexis.sitchler@uwyo.edu)

C. I. Steefel, L. Tomutsa, and L. Yang, Earth Sciences Division, Lawrence Berkeley National Laboratory, 1 Cyclotron Road, Mail Stop 90-1116, Berkeley, CA 94720, USA.